PERGAMON

International Journal of Multiphase Flow 27 (2001) 1109–1126

International Journal of Multiphase Flow

www.elsevier.com/locate/ijmulflow

Effects of liquid viscosity on flow patterns in vertical upward gas–liquid two-phase flow

T. Furukawa [a,*], T. Fukano [b]

[a] *Sasebo College of Technology, Sasebo, Nagasaki 857-1193, Japan*
[b] *Kyushu University, Hakozaki, Fukuaka 812-8581, Japan*

Received 20 December 1999; received in revised form 31 October 2000

Abstract

The purpose of the present experimental study is to investigate the effects of liquid viscosity on the flow patterns of upward air–liquid two-phase flow in a vertical tube of 19.2 mm in inner diameter and about 5.4 m in length. Three different liquids, including water and aqueous glycerol solutions, were employed. Kinematic viscosity of these liquids varied from 1.0×10^{-6} to 14.7×10^{-6} m^2/s. The flow patterns were observed using a video recorder and still photography. The time-spatial characteristic maps of gas–liquid interfaces which were drawn using the mean liquid holdup signals detected by 70 pairs of holdup sensors arranged with the axial spacing of 15 mm over the length of 1.035 m were also used. In this report, we first defined the flow pattern of each flow. Next, the effects of liquid viscosity on the overall flow pattern and interfacial structures, or the interfacial waves, were discussed. Finally, based on those results we proposed flow pattern maps for each liquid viscosity. It is found that the flow pattern transitions strongly depend on the liquid viscosity. © 2001 Elsevier Science Ltd. All rights reserved.

Keywords: Multiphase flow; Interfacial structure; Vertical upward flow; Liquid viscosity; Flow pattern; Large wave; Small wave; Liquid slug

1. Introduction

Gas–liquid two-phase flow phenomena are encountered in various processing industries. The requirements for economic designs, optimization of operating conditions, and assessment of safety operation lead to the need for detailed information on the effects of physical properties of fluids on the flow characteristics of gas–liquid two-phase flow. The knowledge about the effects of physical properties are also important to obtain the fundamental nature of two-phase flow.

* Corresponding author. Tel.: +81-0-956-34-8454; fax: +81-0-956-34-8454.
E-mail address: furukawa@post.cc.sasebo.ac.jp (T. Furukawa).

0301-9322/01/$ - see front matter © 2001 Elsevier Science Ltd. All rights reserved.
PII: S0301-9322(00)00066-5

Generally, the flow characteristics of gas–liquid two-phase flow depend on flow patterns. Therefore, in consideration of the flow characteristics, such as pressure drop for example, it is necessary to know in advance the flow pattern realized under given flow rates conditions.

The flow pattern is influenced by not only each flow rate of both gas and liquid phases, but also physical properties of fluids, flow direction, dimension of flow channel, and so on. The published papers, which discussed the effects of fluid properties, are very few. Only the following examples, i.e., the papers of Baker (1954), Mandhane et al. (1974), Taitel et al. (1978), and Weisman et al. (1979) are pointed out. However, these were for horizontal flow. In addition the discussions about a flow configuration based on detailed observations of the interfacial structures, especially waves on liquid film, and their behaviors were scarcely done.

In the present research, we have investigated the effects of liquid viscosity for vertical upwards flow, and discussed the problem of the flow pattern transitions on the basis of careful observations of the interfacial phenomena. Liquids used in this experiment were water and aqueous glycerol solutions. Liquid viscosity ranged from that of water to 15 times of water, which was almost the same as previous reports (Sekoguchi and Furukawa, 1994; Furukawa, 1995).

Flow patterns were classified based on differences in spatial distributions of both phases or gas–liquid interfacial configurations, which characterize the flow. In the present paper, the flow patterns were discriminated by observing video images, still photography, and time-spatial characteristic map of interfaces obtained from the experiments of a previous paper (Furukawa, 1995).

We first defined flow patterns. Next, the effects of liquid viscosity on the overall flow pattern, interfacial structures and the behaviors of the interfacial waves under typical flow conditions were discussed. Finally, the effects of liquid viscosity on the flow pattern transitions were examined on the basis of the flow pattern maps obtained from these observations for each liquid viscosity.

2. Experimental apparatus and procedure

Fig. 1 shows a schematic diagram of the experimental apparatus. A test section tube with 19.2 mm in internal diameter (D) and about 5.4 m in total length was made of transparent acrylic resin so as to observe the flow pattern. A vertical tube orientation was used. Air and three different liquids, i.e., water and aqueous glycerol solutions with different liquid viscosity, were used as the test fluids. As shown in Table 1, the change in the density (ρ_L) and the surface tension (σ_L) were negligibly small while the viscosity (ν_L) change ranged about 15 times of that of water.

As shown in Fig. 1, air from an air compressor (2) and liquid from a circulation pump (3) were fed into an air–liquid mixer (7) via respective orifice flowmeter (5). The air–liquid mixer consisted of a double tube (80 mm in length), the inner diameter of which was the same as that of the test tube. The air was blown into the inner tube through 48 holes with 2 mm diameter. In the case of lower gas flow rates (superficial air velocity, $j_G \leqslant 2.5$ m/s), an inner tube with holes of 0.3 mm diameter was used.

Two-phase mixture flowed vertically upwards in the test section through a photographing section (8), and was finally introduced into a first separator (9) where the air was released to the atmosphere via a ball valve, which was used in the case of large air flow rate, or a relief valve (16) equipped to keep the system pressure constant, 0.15 MPa in the present experiment. The liquid was returned again to a liquid storage tank (1) through a second separator (11) and a level control valve (10) by which the liquid level in the first separator was controlled. The second separator was

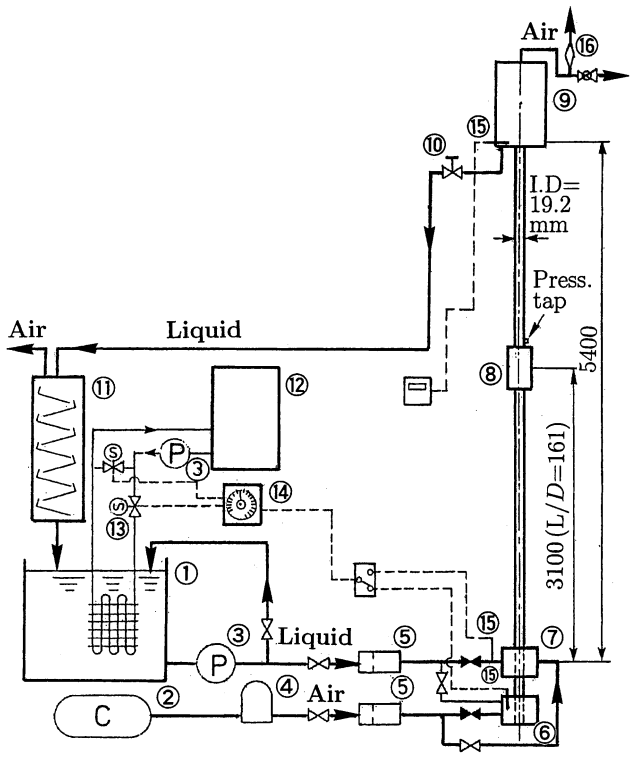

Fig. 1. Schematic diagram of the experimental setup. (1) Liquid storage tank; (2) air compressor; (3) circulation pump; (4) air filter; (5) orifice flowmeter; (6) straightening section; (7) air–liquid mixer; (8) photography section; (9) first separator; (10) level control valve; (11) second separator; (12) water chiller; (13) solenoid-operated valve; (14) temperature control board; (15) resistance thermometer; (16) relief valve.

Table 1
Physical properties of liquids used in the experiments (at $20 \pm 0.1°C$)[a]

Liquid	ν_L (mm^2/s)	ρ_L (kg/M^3)	σ_L (N/m)
Water (W1)	1.0	1000	0.072
53 wt% glycerol solution (G5)	5.7	1125	0.065
72 wt% glycerol solution (G15)	14.7	1172	0.062

[a] ν_L: kinematic viscosity, ρ_L: density, and σ_L: surface tension.

an important device to remove fine bubbles trapped in the liquid phase. The gas bubbles were separated from the thin liquid layer by having the liquid layer flow down in a zigzag passage with changeable slope angles.

The flow characteristics were visually observed, if necessary, by use of both a still camera and a video recorder. The photography section of the flow was located at 3.1 m ($L/D = 161$) downstream of the air–liquid mixer. According to the previous paper (Furukawa, 1991) on the flow development process, this length is enough for flow to fully develop. The photography section was enclosed within a transparent rectangular vessel full of water in order to prevent optical distortions of the flow configuration due to the tube wall curvature.

Liquid temperature in the photography section was estimated by interpolating the liquid temperatures measured at two positions: the first separator and the entrance of the air–liquid mixer or a straightening section (6). Although the difference between two temperatures depended on the gas and liquid flow conditions, it was 1.2°C at the most. Working fluid temperature was kept constant at 20 ± 0.1°C by a water chiller (12).

The experimental conditions were as follows: superficial gas velocity (j_G): $j_G = 0.05$–40 m/s, superficial liquid velocity (j_L): $j_L = 0.1$–1.0 m/s, system pressure (P): $P = 0.15$ MPa, liquid temperature (θ): $\theta = 20 \pm 0.1$°C.

3. Experimental results and discussion

3.1. Definition of flow patterns

The flow patterns were categorized into seven classes on the basis of the visual and video observations and still photography, as well as the time-spatial characteristic map of interfaces obtained from previous experiments (Furukawa, 1995). The flow patterns were defined as follows:

(1) *Bubble flow* (*designated as* **B** *in the following sections*). Small gas bubbles dispersed in a continuum of flowing liquid.

(2) *Bubble-slug flow* (**BS**). This flow is characterized by the non-uniform distribution of the concentration of small bubbles in the flow direction. Small bubble coalescence occasionally occurs in the part of high bubble concentration, and as a result, a spherically capped bubble is formed (see Fig. 3(a)).

(3) *Slug flow* (**S**). This flow pattern is characterized by large bullet shaped bubbles having smooth gas–liquid interface and length longer than a tube diameter, and flowing intermittently with liquid slugs which contain small gas bubbles (see Fig. 3(b) and (c)).

(4) *Slug-froth flow* (**SF**). With an increase in gas flow rate, for example, the gas–liquid interface of the large gas bubble becomes distorted near the nose, but still comparatively smooth in the bottom part of a cylindrical gas bubble (see Fig. 5(1)(c)).

(5) *Froth flow* (**F**). With further increase in gas and liquid flow rates, the gas–liquid interface becomes chaotic and the whole liquid becomes frothy. Oscillating and pulsating behavior characteristics (for example, see Fig. 6(1)(a)) are observed.

(6) *Froth-annular flow* (**FA**). This flow appears if j_G exceeds a certain value under which liquid slugs (LS) disappear, and frothy large waves (LW) pass by intermittently as if they are sliding on the wavy base film with much higher velocity than that of small waves (SW) on the base film (for example, see Fig. 8(1)(a)).

(7) *Annular flow* (**A**). In annular flow the liquid flows on the tube wall as liquid film and the gas phase flows in the center. Usually some of the liquid phase is contained as entrained droplets in the gas core. In the case of extremely high gas flow and low liquid flow, the LW disappear, or the breakdown of the liquid film may occur partially on the tube wall. **A** and **FA** are different in the following respect. In the former case, the LW are relatively uniform in velocities, sizes, and axial spacing while in the latter case those values are scattered. Discrimination of the flow pattern **FA** from **A** is possible to some extent from the video observation. In order to identify features more accurately, the time-spatial characteristic map of interfaces is useful (for example, see Fig. 10(1)(2)(a)).

3.2. Results of flow observations

Flow pattern observations were done under 73 different flow conditions, i.e., superficial velocities of both phases for each v_L. In the following, we will explain the observations of flows under typical flow conditions among these by using the still photographs and the time-spatial characteristic maps of interfaces. The significance of abbreviations described in each figure are as follows. W1: air–water system (kinematic viscosity of liquid $v_L = 1.0 \times 10^{-6}$ m^2/s), G5: air–aqueous glycerol solution system ($v_L \cong 5 \times 10^{-6}$ m^2/s), G15: air–aqueous glycerol solution system ($v_L \cong 15 \times 10^{-6}$ m^2/s), LB: large gas bubble, LS: liquid slug, SW: small wave, FW: flooding wave (explained in detail later), LW: long-life large wave except liquid slug (see Furukawa, 1995).

The flow conditions which correspond to the cases shown in Figs. 3–10 are shown by ◯ in Fig. 2.

3.2.1. Flow in developing region

Fig. 3 shows the still photographs of the three fluids under the same flow condition ($j_G = 0.2$ m/s, $j_L = 0.3$ m/s). In the case of W1, as shown in Fig. 3(a), agglomeration or coalescence of small bubbles is occasionally observed. The upper and lower parts of Fig. 3(a) for example, signify that the flow is in the transition region from the bubble flow to the slug flow. Meanwhile, the flow pattern of G5 and G15 shown in Fig. 3(b) and (c) are typical slug flow. Large gas bubbles (LB) in both cases have almost the same bullet shape as well as the same nose curvature, except that the liquid film around LB for G15 is thicker than that for G5 due to the larger viscosity. Although small bubbles of the order of 1 mm in diameter are observed in the liquid film and liquid slug, the bubble concentration is low. And therefore, the gas–liquid interface is smooth and the tube section appears to be transparent.

As described above, the flow pattern of W1 differs from those of G5 or G15 even if the gas and liquid flow rates condition is the same. This implies that the air and liquid flow rates condition for

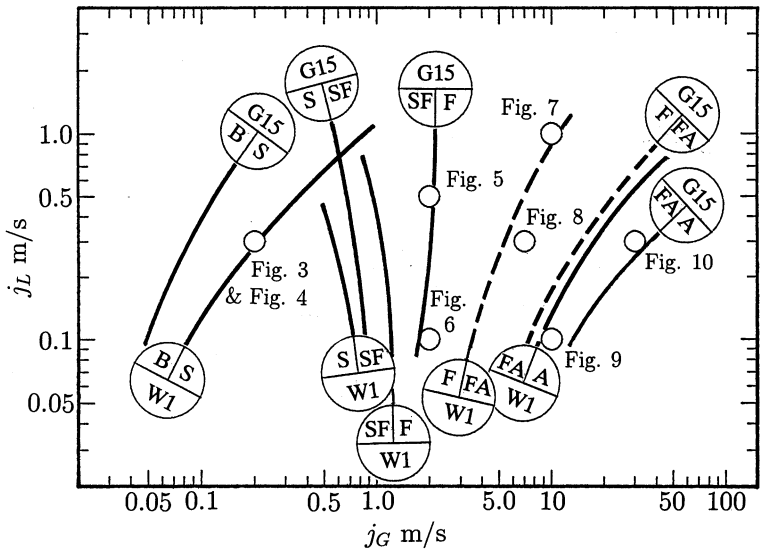

Fig. 2. Experimental points (◯) which are shown in Figs. 3–10.

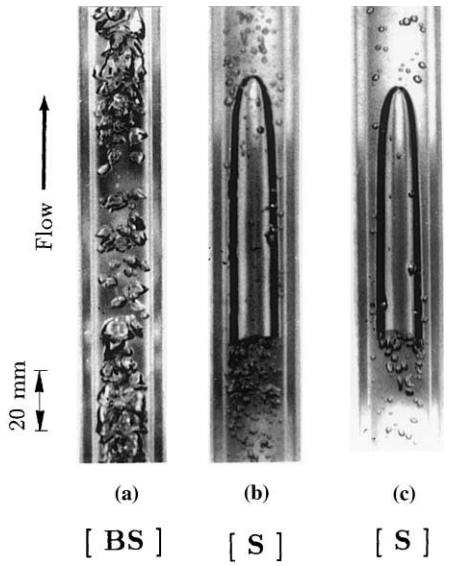

Fig. 3. Examples of the difference in flow patterns at the same flow conditions ($j_G = 0.2$ m/s, $j_L = 0.3$ m/s). (a) W1; (b) G5; (c) G15.

transition from the bubble flow to the slug flow depends on v_L, and that small bubble coalescence is easy to occur in the case of larger v_L.

In order to confirm the effect of viscosity on the developing flow configuration, i.e., to know the location where small bubbles coalesce into larger gas bubbles, detailed observation of flow was done in the region downstream of the gas–liquid mixer. Fig. 4 shows the developing flow field at three different axial locations; at the gas–liquid mixer, at $L = 0.5$ m, and at 1 m downstream of the mixer for each case of W1 (Fig. 4(a)) and G5 (Fig. 4(b)). The flow condition is the same as that in Fig. 3.

As shown in Fig. 4, in both cases of W1 and G5, small bubbles with nearly the same diameter are formed at the gas–liquid mixer without bubble coalescence, and flow configurations at this section scarcely differ. In case of G5, the bubble flow (**B**) continues up to at least $L \cong 0.5$ m. And bubble coalescence begins at $L \cong 1$ m. On the other hand, for the case of W1, although the number of bubbles slightly decreases due to bubble coalescence, LB do not appear because of infrequent bubble coalescence. Therefore, the bubble flow still exists at $L = 1$ m position. As described above, it is concluded that the difference of the flow configuration as shown in Fig. 3 is not caused by the gas–liquid mixer, but by the difference in degree of coalescence of small bubbles in the flow downstream of the mixer, and that the distance from the mixer to the position of the large gas bubble generation decreases with increasing v_L.

3.2.2. Flow in comparatively small j_G region

Fig. 5 shows the comparison of the typical still photograph (Fig. 5(1)) and the time-spatial characteristic map of interfaces (Fig. 5(2)) for each v_L, in which time-varying signals of the cross-sectional mean liquid holdup (η signal) detected at 70 axially different cross-sections in 1.035 m tube length were recorded (Furukawa, 1995). The flow condition was $j_G = 2.0$ m/s and $j_L = 0.5$ m/s. Fig. 5(1) indicates that the larger the value of v_L, smaller and more numerous

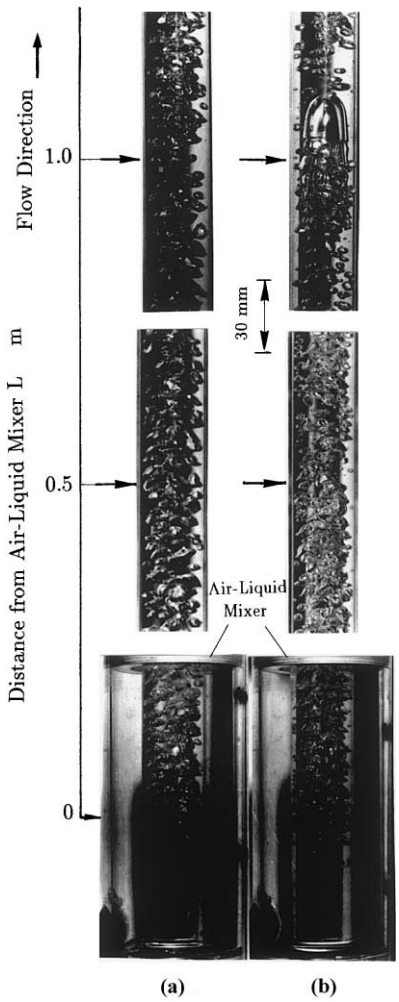

Fig. 4. Effects of liquid viscosity on bubble coalescence ($j_G = 0.2$ m/s, $j_L = 0.3$ m/s). (a) W1; (b) G5.

bubbles are included in the liquid film around LB and LS. In addition, the liquid film thickness becomes larger as viscosity increases. This is shown more clearly in the time-spatial characteristic map shown in Fig. 5(2). That is, the values of η around the LB become larger as v_L increases. In Fig. 5(2), the trapezoidal shape of waves in η signals indicate liquid slug (LS) and it can be seen that passing frequency of LS increases with increasing v_L. Although the lengths of LB and LS become shorter according as v_L increases, coalescence between LB can be scarcely seen, so it is considered that the flow is stable even in the G15 case. The number of SW formed on the liquid film surrounding LB between two LSs decreases as v_L increases. In case of G15, SW can be only slightly seen in Fig. 5(2). From this fact, it is concluded that the smaller the v_L, the larger the waviness of interface.

In the bottom part of a large gas bubble, a liquid film absolutely flows downwards if the bubble is long enough (Fukano et al., 1981). In Fig. 5(2), we can see the traces of negative gradient for

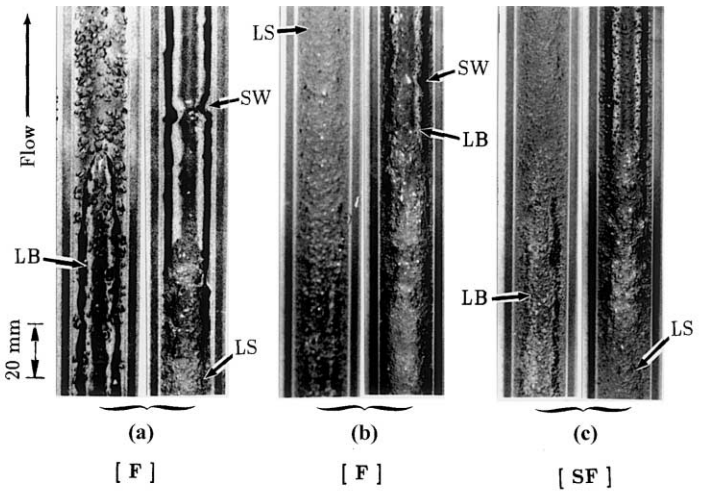

(1) Characteristics of interfaces for each liquid viscosity.

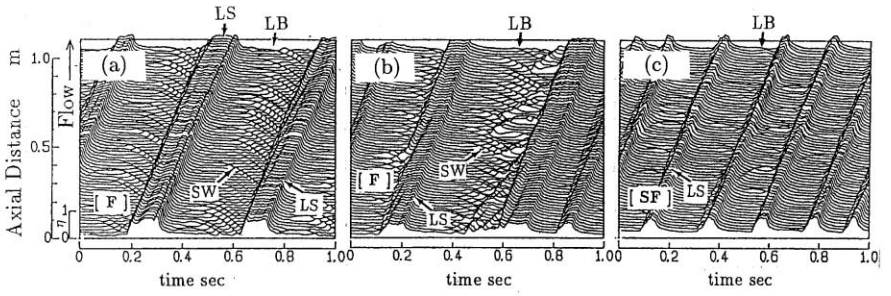

(2) Comparison of time-spatial characteristic map of interfaces for each liquid viscosity.

Fig. 5. Effects of liquid viscosity on interfacial structures and behaviors of interfacial waves at the same gas and liquid flow rates ($j_G = 2.0$ m/s, $j_L = 0.5$ m/s). (a) W1; (b) G5; (c) G15.

SWs in the cases of W1 and G5, i.e., the SWs move reversibly to the main flow direction as time proceeds. This indicates that the SW move with falling liquid film around a large gas bubble in its rear part. The actual shape of these SW seems to be tear-dropwise as shown with arrows in Fig. 5(1). In case of G15, the falling film portion is limited due to that the large gas bubble is short as shown clearly in Fig. 5(2)(c), therefore falling SW is scarcely observed.

Considering the above observation of the time-spatial characteristic maps and the all still photographs, it is judged that the flow pattern of W1 and G5 is froth flow (**F**), and that of G15 is the slug-froth flow (**SF**).

Fig. 6 shows the flow in the case of $j_L = 0.1$ m/s under the same j_G condition, 2.0 m/s, as that shown in Fig. 5. As is obvious from the still photographs indicated in Fig. 6(1), the flow patterns of W1, G5, and G15 are judged, according to the previous definition, as the typical froth flow for the reason that the gas–liquid interfaces are so complicated for any value of v_L. It is noticed that many small bubbles are scattered in the nose part of LB and coalesce into the large gas bubble while flowing (see photograph of the left-hand side of Fig. 6(1)(a)). Therefore, in the bottom part

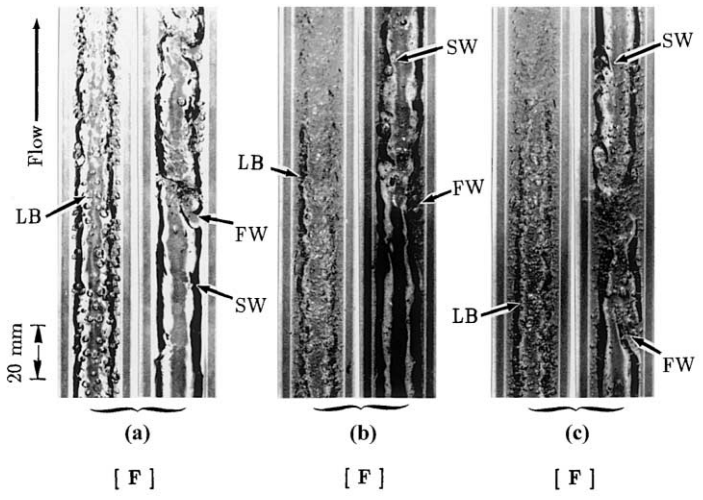

(1) Characteristics of interfaces for each liquid viscosity.

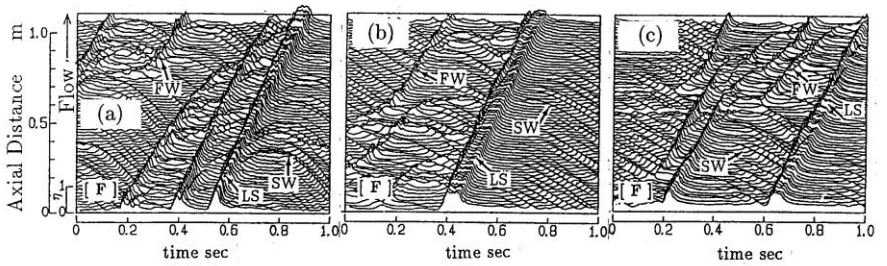

(2) Comparison of time-spatial characteristic map of interfaces for each liquid viscosity.

Fig. 6. Effects of liquid viscosity on interfacial structures and behaviors of interfacial waves at the same gas and liquid flow rates ($j_G = 2.0$ m/s, $j_L = 0.1$ m/s). (a) W1; (b) G5; (c) G15.

of the liquid film, the small bubbles can be scarcely observed (photograph on the right-hand side of Fig. 6(1)(a)). Meanwhile in the case of G5 and G15, a large number of small bubbles with diameters below 1 mm are contained over the entire flow field. Therefore, the transparent liquid film and the frothy liquid slug flow alternately in the case of W1, whilst the whole tube looks cloudy in the cases of G5 and G15. Even so, it is possible to observe the existence of the waves (LW, FW) and the behavior of these waves and LS, because these are cloudier than the liquid film.

As is shown in Fig. 6(2), the downward movements of SW formed on the falling liquid film around the LBs are sometimes prevented by the interfacial shear force induced by up-going gas flow. The SW grow by coalescence of successively falling SW. The grown-up LW are referred to as the flooding wave (FW) in the present paper, the examples of which are pointed with arrows in Figs. 6(1) and (2). This FW, which oscillates to and fro within the tube and shows very unstable behaviors, is usually absorbed into the following up-going LW or LS, and disappears as clearly shown in the cases of G5 and G15 of Fig. 6(2), or it grows into a larger wave as seen in W1 in Fig. 6(2). The behaviors of FW were observed in each case of v_L. This wave is considered to be similar to the suspending wave which has been pointed out by one of the authors as the trigger-wave

which develops into a disturbance wave in the annular flow region (Fukano et al., 1987). In the vicinity of this flow condition with $j_G = 2.0$ m/s and $j_L = 0.1$ m/s, the flooding waves appear most frequently because the large scale flow reversal with considerably thick film occurs. As can be seen from the gradient of the traces of SWs, in Fig. 6(2), the falling velocity of SW formed on the liquid film decreases with increasing v_L. The reason for this is due to lower downward velocities caused by higher viscous forces, and because the length of the large gas bubble becomes shorter with increasing v_L as mentioned before.

3.2.3. Flow in the case of large j_G and j_L

Fig. 7 shows the flow under the flow condition with large j_G and j_L, $j_G = 10$ m/s and $j_L = 1.0$ m/s, for example. The flow pattern is the froth flow for all cases of v_L in this flow condition. According to the visual and video observations, the flow appears to be cloudy independently of v_L, and it is very difficult to discriminate the wave configuration in the core of the tube.

The left-hand side photographs of Fig. 7(1) for each v_L show the instant the LS or LW pass by the photography section. Under the flow condition with large j_L as shown here, it is difficult to

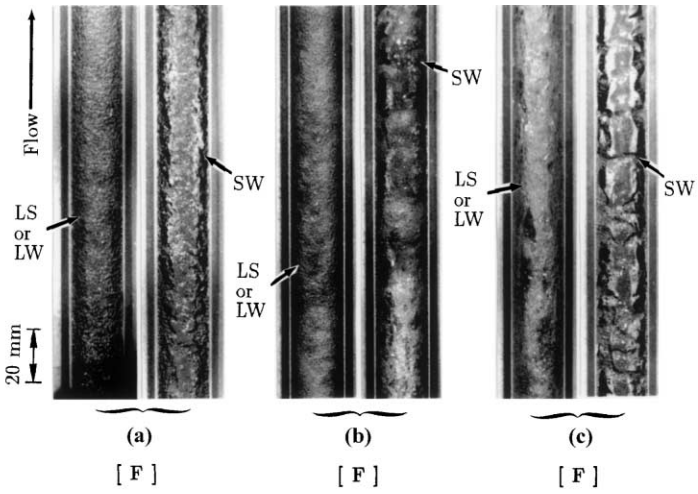

(1) Characteristics of interfaces for each liquid viscosity.

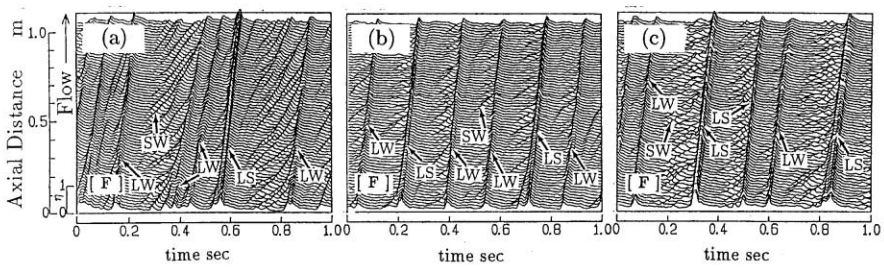

(2) Comparison of time-spatial characteristic map of interfaces for each liquid viscosity.

Fig. 7. Effects of liquid viscosity on interfacial structures and behaviors of interfacial waves at the same gas and liquid flow rates ($j_G = 10$ m/s, $j_L = 1.0$ m/s). (a) W1; (b) G5; (c) G15.

judge quantitatively the effects of v_L on the size and the concentration of small bubbles contained in LS and LW. On the other hand, the right-hand side photograph shows the liquid film. This photograph represents that the size of the SW formed on the liquid film becomes larger as v_L increases. And velocity of SW decreases with increasing v_L, as can be understood if compared with the gradient of traces for SW shown in each Fig. 7(2)(a), (b), and (c).

We notice in Fig. 7(2) that the number of LS increases as v_L is increased. Contrary to this, the number of LW decreases with increasing v_L. Therefore, it can be understood that the flow becomes closer to the froth-annular flow (**FA**) with decreasing v_L. The distinction between LS and LW was made based on their velocities, i.e., LS has the velocity nearly equal to the value obtained from the correlation proposed by Nicklin et al. (1962) for LB, and LW has the velocity less than this. The velocity was obtained by reading the gradient of traces of LS or LW in the enlarged Fig. 7(2). For example, the velocities of liquid lumps obtained for G5 in Fig. 7(2)(b) were 9.34 (LW), 12.89 (LS), 9.29 (LW), 8.22 (LW), 12.82 (LS), and 11.67 (LW) m/s in order from the left-hand side.

3.2.4. Flow in the vicinity of *FA*

Fig. 8 shows the flow for $j_G = 7$ m/s and $j_L = 0.3$ m/s. As previously reported (Furukawa, 1995) and understood from the gradient of the waves in Fig. 8(2)(a), LS disappears under this flow condition in the case of W1. Therefore, the flow pattern may be identified to be either the froth-annular flow (**FA**) or the annular flow (**A**). However, as shown in Fig. 8(2)(a), velocity, size, and axial spacing of LW are not uniform, therefore the flow pattern of this flow is judged as the **FA**. Flow pattern in the cases of G5 and G15 is the froth flow because LSs exist as clearly shown in Fig. 8(2)(a) and (b).

Fig. 8(1) and (2) clearly show that the size of SW formed on the liquid film becomes larger with increasing v_L. Also, SWs move upward, signifying that no downward flow of liquid film occurs. Close inspection of Fig. 8(1) and careful observation of the flow reveal that in the cases of G5 and G15 a large number of very small bubbles (below 1 mm in dia.) are contained in the liquid film, but not in W1. The reason why there are less bubbles in the film is that the small bubbles collapse easily into a large bubble because the liquid film is thinner than the bubble diameter in the case of W1. As a result the liquid film in this case appears to be transparent. On the other hand, in cases of G5 and G15, the liquid film is semitransparent due to mixing of very fine bubbles.

The cloudy liquid lumps flowing as if, visually, they are sliding on the liquid film are LSs or LWs, which are pointed by arrows in Fig. 8(1) and (2). Close inspection of the flow recorded on the video recorder as well as Fig. 8(2) reveals that as v_L is increased those liquid lumps decrease in the passing frequency, but increase in the velocity and the size, with the flow structure being more stable and fully developed.

As discussed above, it is concluded that the flow structure is strongly dependent on v_L.

3.2.5. Flow close to annular flow

Fig. 9 shows the flow phenomena under the flow condition of $j_G = 10$ m/s and $j_L = 0.1$ m/s. In this flow condition, the existence of LS cannot be confirmed independently of the magnitude of v_L (Furukawa, 1995). As seen in Fig. 9(2)(a), the flow pattern in the case of W1 is judged as the annular flow (**A**), because the velocity, size, and axial spacing of LW are nearly uniform. On the other hand, LW of G5 (Fig. 9(2)(b)) and G15 (Fig. 9(2)(c)) are not uniform in the velocity, size,

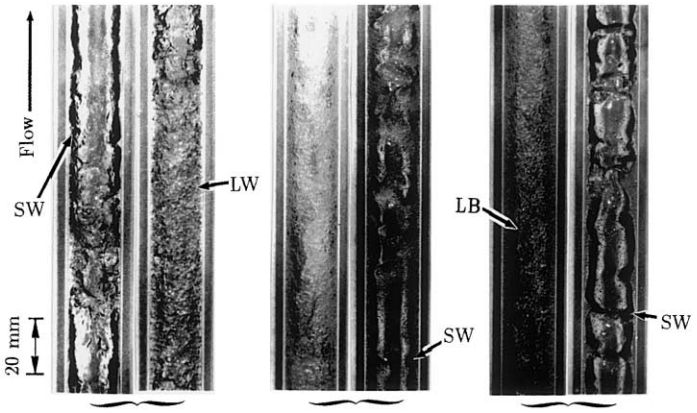

(1) Characteristics of interfaces for each liquid viscosity.

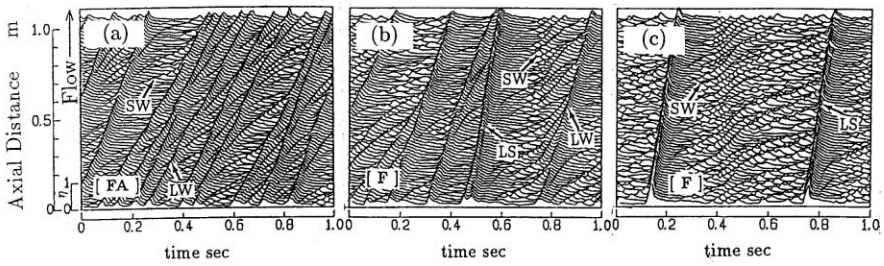

(2) Comparison of time-spatial characteristic map of interfaces for each liquid viscosity.

Fig. 8. Effects of liquid viscosity on interfacial structures and behaviors of interfacial waves at the same gas and liquid flow rates ($j_G = 7.0$ m/s, $j_L = 0.3$ m/s). (a) W1; (b) G5; (c) G15.

and axial spacing, so that these flows should not be judged as **A**. In this paper, such flows are referred to as the froth-annular flow (**FA**) as mentioned in Section 3.1.

As can be seen in Fig. 9(1) and (2), gas–liquid interfacial structures of liquid film strongly depend on the value of v_L. That is, in case of W1 the liquid film, where SWs are barely observed, is thin. Also, the interface is relatively smooth, while in case of G15 the liquid film thickness and the scale of SW becomes larger, and its interface appears to be extremely wavy.

Fig. 10 shows the flow under a much higher air flow rate and larger liquid flow rate than those shown in Fig. 9, i.e., $j_G = 30$ m/s, $j_L = 0.3$ m/s. The flow for W1 shown in Figs. 10(1)(a) and (2)(a) is the fully developed annular flow. The LWs in this flow are usually referred to as disturbance waves, which should have approximately uniform velocity, size, and axial spacing (Sekoguchi et al., 1973). Similar wave characteristics are observed in case G5 as shown in Fig. 10(2)(b). The flow pattern in case G5 is also judged as the fully developed annular flow. The disturbance waves in this case are approximately 30 mm in flow direction as can be seen in Figs. 10(1)(a) or (b), and move as if they slide on the liquid film. In addition, as seen in Fig. 10(2)(a) or (b), the η signal

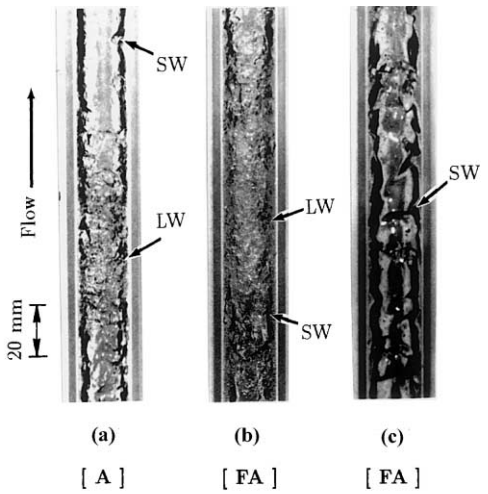

(1) Characteristics of interfaces for each liquid viscosity.

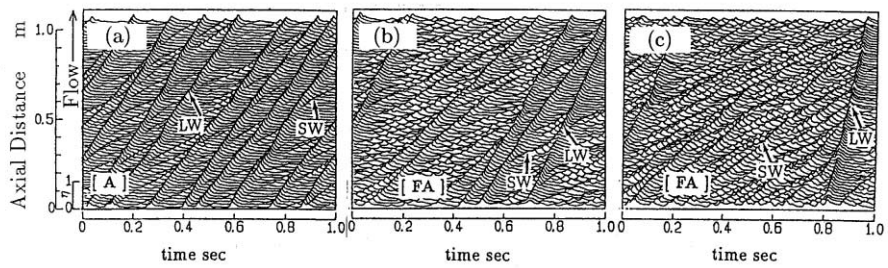

(2) Comparison of time-spatial characteristic map of interfaces for each liquid viscosity.

Fig. 9. Effects of liquid viscosity on interfacial structures and behaviors of interfacial waves at the same gas and liquid flow rates ($j_G = 10$ m/s, $j_L = 0.1$ m/s). (a) W1; (b) G5; (c) G15.

shows that the wave structure scarcely changes while flowing over the observation section of about 1 m.

On the other hand, in the case of G15 shown in Fig. 10(2)(c), the uniformity in velocity, size, axial spacing of LW is deteriorated, which is different from the characteristics of disturbance waves in the cases of W1 and G5 as described above. Therefore, the flow pattern in the case of G15 with this flow condition is judged to be the froth-annular flow (**FA**).

It is revealed from Figs. 10(1) and (2) that as v_L is increased, the gas–liquid interface changes from relatively smooth to intensively wavy. In addition, as is evident from Figs. 10(1) and 9(2), the values of holdup η, which correspond to the liquid film, increase with increasing v_L, signifying that the liquid film thickness increases with increasing v_L. Furthermore, Fig. 10(2) represents that the passing frequency of LW decreases with increasing v_L. Those data suggest that the mechanism of liquid transport is dependent upon v_L. That is, as v_L increases, the ratio of the liquid flow rate transported by LW decreases, and the liquid transport by the base film increases.

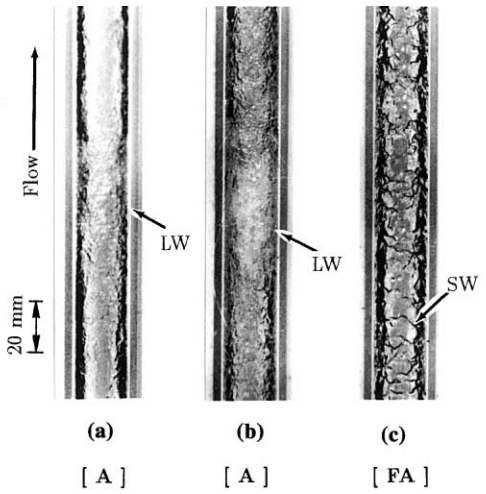

(1) Characteristics of interfaces for each liquid viscosity.

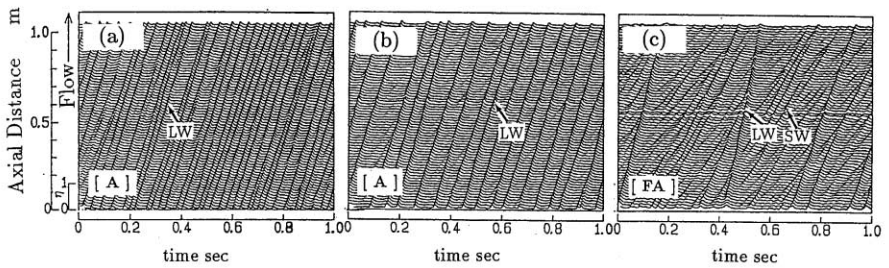

(2) Comparison of time-spatial characteristic map of interfaces for each liquid viscosity.

Fig. 10. Effects of liquid viscosity on interfacial structures and behaviors of interfacial waves at the same gas and liquid flow rates ($j_G = 30$ m/s, $j_L = 0.3$ m/s). (a) W1; (b) G5; (c) G15.

3.3. Flow pattern maps

Fig. 11 shows the flow pattern maps obtained by taking into account all the data, such as the video images, the still photographs, and the time-spatial characteristic maps as well as the visual observations, as described in Section 3.2. In these maps, the flow patterns are noted by abbreviated letters. Fig. 11(a), (b), and (c) correspond to the cases of W1, G5, and G15, respectively. In each figure, the boundaries of the flow patterns are represented by the thick solid lines, and the disappearance region of liquid slug is divided by the thick broken lines. Again, the solid symbols indicate the experimental points, in which falling film surrounding the large gas bubble was observed, and double circle symbols with solid mark represent experimental points, in which falling film and flooding waves occurred at the same time.

For comparison, the following equation proposed by Govier (1972) for the condition of transition of flow pattern from the bubble flow (**B**) to the slug flow (**S**) is expressed by thin one-dot chain lines in Fig. 11

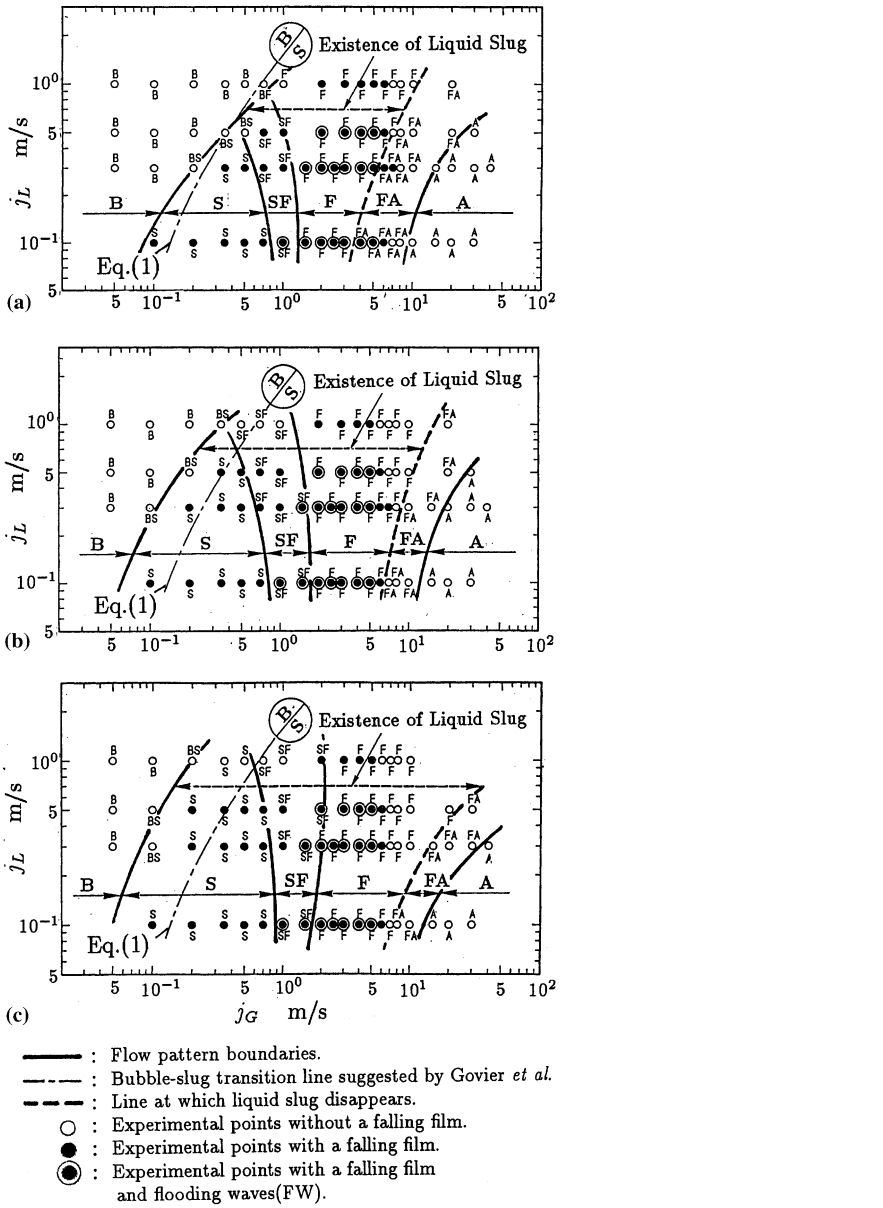

Fig. 11. Effects of liquid viscosity on flow pattern maps. (a) W1; (b) G5; (c) G15.

$$j_G = 0.56 j_L + 0.16\sqrt{\frac{gD(\rho_L - \rho_G)}{\rho_L}}, \tag{1}$$

where D is the inside diameter of tube, g the gravitational acceleration, ρ_G and ρ_L are the gas and liquid density, respectively. This equation has been obtained by taking into account the conservation of gas volume flow rate of large and small gas bubbles in the liquid slug and using the rising velocity

of a large gas bubble (u_G) expressed by Eq. (2) (Nicklin et al., 1962; Zuber and Findlay, 1965). They assumed that the slug flow was characterized by the existence of large gas bubble longer than the inside diameter of tube (for example, the state as seen in photograph at $L = 1$ m in Fig. 4(b)).

Eq. (1) can be derived also by using Eq. (2) and the fact that the transition from **B** to **S** occurs when the averaged void fraction $\hat{\alpha}$ becomes 0.3 (Mishima and Ishii (1984))

$$u_G = 1.2(j_G + j_L) + 0.35\sqrt{\frac{gD(\rho_G - \rho_L)}{\rho_L}}, \tag{2}$$

$$u_G = j_G/\hat{\alpha}. \tag{3}$$

Note that the bubble-slug transition line of Eq. (1) is also the contour line of $\hat{\alpha} = 0.3$ for at least air–water system.

The transition lines from **B** to **S** will be discussed first. In the case of W1 shown in Fig. 11(a), this transition line agrees well with the curve of Eq. (1), i.e., the curve of $\hat{\alpha} = 0.3$. As v_L increases (see G5 and G15), the agreement with Eq. (1) becomes worse, i.e., the transition lines from **B** to **S** considerably shift to smaller j_G. This physically means that if the relative velocity between gas and liquid is independent of v_L, the value of $\hat{\alpha}$ at the **B–S** transition noticeably decreases with v_L. On the contrary, if the **B–S** transition occurs independently of v_L at nearly $\hat{\alpha} = 0.3$, it means that the relative velocity between gas and liquid decreases with increasing v_L.

Next, the transition from the froth flow (**F**) to the froth-annular flow (**FA**), which corresponds to the thick broken line at which LS disappear, shifts to a higher j_G region with increasing v_L (Furukawa, 1995). The transition from **FA** to annular flow (**A**) also moves to the higher j_G region as v_L is increased. Thus the range of existence of LS, which is shown by thin horizontal broken lines, becomes wider with increasing v_L.

As mentioned above, the demarcation lines of flow patterns, which are plotted on j_G–j_L map, are strongly dependent on viscosity v_L.

It is noticed that the solid marks, which show the existence of the falling liquid film and flooding waves, are distributed almost independently of the magnitude of v_L, and that both the falling liquid film and the flooding waves occur most vigorously under the condition around $j_G = 2$–2.5 m/s.

3.4. Rearrangement of flow pattern map by using Baker's parameters

As to the flow pattern map, in which the effect of physical properties of fluids are taken into consideration, Taitel and Dukler (1976) and Taitel et al. (1978) proposed parameters which include the physical properties of fluids based on the theoretical investigation on the transition of the flow patterns, and compared with the published data. Flow pattern transitions were also discussed by Mandhane et al. (1974) by plotting the experimental data taken by Baker (1954) and other researchers on j_G–j_L map. These discussions, however, were not for vertical upward flow as in the present paper, but for horizontal flow. In the present paper, Baker's parameters were examined if they are applicable to the vertical upward flow with different viscosity. In Baker map, the ordinate axis is the ratio of mass flow rate of gas (G_G) to parameter λ, and the abscissa is the product of three values: the ratio of mass flow rate of liquid (G_L) to G_G, (G_L/G_G), parameters λ and ψ, where λ and ψ are defined as follows:

$$\lambda = \{(\rho_G/\rho_A)(\rho_L/\rho_W)\}^{1/2}, \tag{4}$$

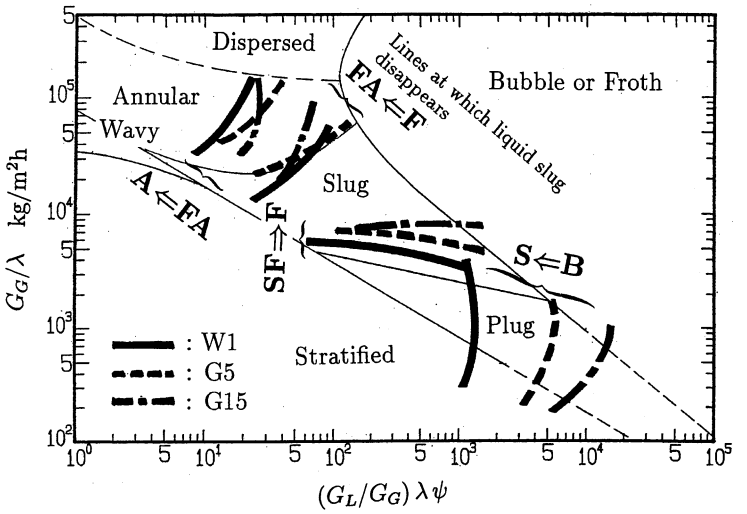

Fig. 12. The flow pattern transition lines drawn on Baker map.

$$\psi = (\sigma_W/\sigma_L)\{(\nu_L/\nu_W)(\rho_W/\rho_L)\}^{1/3}, \tag{5}$$

where ρ is the density, σ the surface tension and ν is the kinematic viscosity. The subscripts L, W, G, and A mean liquid, water at 20°C, gas, and air at 20°C, respectively.

The boundary lines of flow patterns already shown in Fig. 11 for each liquid viscosity are drawn on the Baker map as shown in Fig. 12. The thick solid lines, the broken lines, and the one-dot chain lines represent the boundaries for the cases of W1, G5, and G15, respectively.

From Fig. 12, it is noticed that the boundary lines of **B** and **S** shift considerably to the left side with increasing ν_L. On the other hand, the boundary lines of **F** and **FA** as well as **FA** and **A** are relatively gathered with each other independently of ν_L, which signifies that those transition lines are improved by using Baker's coordinates rather than by superficial velocities in Fig. 11, while the transition lines between **B** and **S** does not.

Comparison of the Baker map with the present boundary lines reveals that (1) the similarity of the boundary lines between **B** and **S** cannot be expressed by Baker's parameters, (2) the tendency of the boundary lines between **SF** and **F** is similar to the case of horizontal flow, although the present results are located somewhat upward of the boundary line between the plug and slug flow in horizontal flow, (3) the boundary lines between **F** and **FA**, i.e., the disappearance lines of LS, agree well with the boundary line between the slug and annular flow in horizontal flow. This fact suggests that the disappearance of large LS is controlled, at least partially, by Baker's parameters irrespective of the orientation of pipe line.

4. Conclusions

The effects of liquid viscosity upon the transition of the flow pattern were experimentally investigated. The experiments were carried out using water and aqueous glycerol solutions as working liquids with up to 15 times change in liquid viscosity for isothermal, co-current, air–liquid, vertical upward flow in a 19.2 mm inner diameter tube. The results obtained are summarized as follows:

(1) Liquid viscosity (v_L) significantly affects the structures of the liquid film surrounding LB in slug flow, and also those of waves formed on the liquid film in annular flow.
(2) The flow pattern maps presented by using the superficial velocities of both phases, j_G and j_L, as the coordinate axes were obtained for three different kinds of liquid viscosities.
(3) From the flow pattern maps obtained, the following are pointed out:
(a) The transition line from bubble flow to slug flow significantly shifts to the smaller j_G region with increasing v_L.
(b) Both the transition lines from the froth flow to the froth-annular flow and from the froth-annular flow to the annular flow move to the larger j_G region with increasing v_L.
(c) The falling liquid film around the large gas bubble and flooding wave appear at nearly the same gas and liquid flow rates, independently of v_L.
(d) By using Baker's coordinates, the boundary lines between the froth flow and the froth-annular flow, and the froth-annular flow and the annular flow are correlated comparatively well, but it is not possible to correlate the boundary between the bubble flow and the slug flow.

Acknowledgements

The authors wish to express their appreciation to N. Okamoto and S. Kimura, students of Sasebo National College of Technology at that time, for their cooperation in the experiment.

References

Baker, O., 1954. Simultaneous flow of oil and gas. Oil Gas J. 53, 185–190.
Fukano, T., Matumura, K., Kawakami, Y., Sekoguchi, K., 1981. Transient behavior of a gas slug, second report – on the liquid film thickness around a gas slug. Bull. Jpn. Soc. Mech. Eng. 24, 1440–1447.
Fukano, T., Kawakami, Y., Itoh, A., Tominaga, A., 1987. Mechanism of the disturbance wave generation in a vertical up- and down-ward gas–liquid two-phase annular flow. Transient Phenomena in Multiphase Flow Hemisphere, 435–452.
Furukawa, T., 1991. Study on flow developing process in upward gas–liquid two-phase flow. Research Reports of Sasebo College of Technology 28, 5–20.
Furukawa, T., 1995. Effect of liquid viscosity on liquid-lump velocity in vertical upward gas–liquid two-phase flow, velocity characteristics of the long-life liquid lump. Jpn. J. Multiphase Flow. 9, 121–131.
Govier, G.W. (Ed.), 1972. The Flow of Complex Mixtures in Pipes. Van Nostrand Reinhold, New York, pp. 388–389.
Mandhane, J.M., Gregory, G.A., Aziz, K., 1974. A flow pattern map for gas–liquid flow in horizontal pipes. Int. J. Multiphase Flow 1, 537–553.
Mishima, K., Ishii, M., 1984. Flow regime transition criteria for upward two-phase flow in vertical tubes. Int. J. Heat Mass Transfer 27, 723–737.
Nicklin, D.J., Wilkes, J.O., Davidson, J.F., 1962. Two-phase flow in vertical tubes. Trans. Int. Chem. Eng. 40, 61–68.
Sekoguchi, K., Nishikawa, K., Nakasatomi, M., Nishi, H., Kaneuzi, A., 1973. Liquid film flow phenomena in upward two-phase annular flow. Trans. Jpn. Soc. Mech. Eng. 39, 313–323.
Sekoguchi, K., Furukawa, T., 1994. Effect of liquid viscosity on liquid lump velocity in vertical upward gas–liquid two-phase flow, first report, mean liquid lump velocity and its standard deviation. Trans. Jpn. Soc. Mech. Eng. B 60, 552–559.
Taitel, Y., Dukler, A.E., 1976. A model for predicting flow regime transitions in horizontal and near horizontal gas–liquid flow. AIChE J. 22, 47–55.
Taitel, Y., Lee, N., Dukler, A.E., 1978. Transient gas–liquid flow in horizontal pipes: modeling the flow pattern transitions. AIChE J. 24, 920–934.
Weisman, J., Duncan, D., Gibson, J., Crawford, T., 1979. Effects of fluid properties and pipe diameter on two-phase flow patterns in horizontal lines. Int. J. Multiphase Flow 5, 437–462.
Zuber, N., Findlay, J.A., 1965. Average volumetric concentration in two-phase flow systems. Trans. ASME J. Heat Transfer Ser. C 87, 453–463.